Modular Self-Assembling Dendrimer Nanosystems for Magnetic Resonance And Multimodality Imaging of Tumors

Ling Ding, Zhenbin Lyu, Teodora-adriana Perles-Barbacaru, Adela Ya-ting Huang, Baoping Lian, Yifan Jiang, Tom Roussel, Christina Galanakou, Suzanne Giorgio, Chai-lin Kao, et al.

Modular self-assembling dendrimer nanosystems for magnetic resonance and multimodality imaging of tumors

Ling DING[1,2], Zhenbin LYU[1], Teodora-Adriana PERLES-BARBACARU[2], Adela Ya-Ting HUANG[1,3], Baoping LIAN[4], Yifan JIANG[1], Tom ROUSSEL[1], Christina GALANAKOU[1], Suzanne GIORGIO[1], Chai-Lin KAO[3], Xiaoxuan LIU[4], Juan IOVANNA[5], Monique BERNARD[2], Angèle VIOLA[2], Ling PENG[1]

[1] Aix Marseille University, CNRS, Centre Interdisciplinaire de Nanoscience de Marseille (UMR 7325), Equipe Labellisée Ligue Contre le Cancer, Marseille, France

[2] Aix Marseille University, CNRS, Centre de Résonance Magnétique Biologique et Médicale (CRMBM), UMR 7339 Marseille 13385, France

[3] Department of Medicinal and Applied Chemistry, Drug Development and Value Creation Research Center, Kaohsiung Medical University, 100 Shih-Chuan 1st Road, 80708 Kaohsiung, Taiwan

[4] State Key Laboratory of Natural Medicines and Jiangsu Key Laboratory of Drug Discovery for Metabolic Diseases, Center of Drug Discovery, Center of Advanced Pharmaceuticals and Biomaterials, China Pharmaceutical University, Nanjing, P. R. China

[5] Centre de Recherche en Cancérologie de Marseille, INSERM U1068, CNRS, UMR 7258, Institut Paoli-Calmettes, Aix Marseille Université, 13273 Marseille, France

E-mail: ling.peng@univ-amu.fr

Abstract

Bioimaging is a powerful tool for diagnosing tumors but remains limited in terms of sensitivity and specificity. Nanotechnology-based imaging probes able to accommodate abundant imaging units with different imaging modalities are particularly promising for overcoming these limitations. In addition, the nanosized imaging agents can specifically increase the contrast of tumors by exploiting the enhanced permeability and retention effect. We performed a proof-of-concept study on pancreatic cancer to demonstrate the use of modular amphiphilic dendrimer-based nanoprobes for magnetic resonance imaging (MRI) or MR/near-infrared fluorescence (NIRF) multimodality imaging of tumors. Specifically, self-assembly of an amphiphilic dendrimer bearing multiple Gd^{3+} contrast units at its terminals, generated a nanomicellar agent exhibiting favorable relaxivity for MRI with a good safety profile. MRI revealed an up to 2-fold higher contrast enhancement in tumors than in normal muscle. Encapsulating the NIRF dye within the core of the nanoprobe yielded an MR/NIRF bimodal imaging agent for tumor detection that was efficient both for MRI, at Gd^{3+} concentrations 1/10 the standard clinical dose, and for NIRF imaging, allowing over two-fold stronger fluorescence intensities. These self-assembling dendrimer nanosystems thus constitute effective probes for MRI and MR/NIRF multimodality imaging, and offer a promising nanotechnology platform for elaborating multimodality imaging probes in biomedical applications.

Keywords:

Self-assembly; dendrimer; MRI; NIRF imaging, pancreatic cancer

Introduction

Cancer is one of the leading causes of death worldwide and remains a difficult disease to treat. Early and accurate diagnosis positively influences the effective management of cancer. It provides the opportunity to intervene during the early stages of disease, leading to more effective treatment, increased survival rates, and in some cases even a complete cure. In this context, bioimaging plays an important role in cancer diagnosis, by allowing non-invasive tumor detection and staging, as well as an assessment of treatment efficacy.[1,2] However, bioimaging remains limited in terms of sensitivity, specificity and accuracy, as well as toxicity associated with certain imaging agents.

The application of nanotechnology to bioimaging offers the potential to overcome some or all of these limitations.[3,4] Specifically, nanosized agents can carry an abundance of imaging reporters, thereby significantly improving imaging sensitivity. In addition, nanotechnology allows the combining of different imaging modalities within the same nanosystem. This enables multimodality imaging that provides more precise and complete information compared to that obtained using single modality imaging. Furthermore, nanosized agents may home in on and accumulate within tumors by way of the "enhanced permeability and retention (EPR)" effect.[5-10] This effect is based on the leaky vasculature and dysfunctional lymphatic drainage found in the tumor microenvironment. This enables the accumulation of the nanosized agents within the tumor, thereby improving imaging sensitivity and specificity for cancer diagnosis. Clinical studies have confirmed the existence of the EPR effect within certain human tumors, however the relevance of the EPR phenomenon occurring for all nanoparticles and in all patients and tumors is now debated.[11-13] Recent studies show that tumor vascular permeability represents a dynamic phenomenon that can promote nanoparticle delivery.[14] In addition, some inorganic nanoparticles can even directly produce gaps on the tumor vessel wall thereby generating the vascular leakiness required to produce the EPR effect.[15] Also, tumor targeting based on transcytosis[16,17] and in situ tumor-

generated extracellular vesicle-mediated delivery[18,19] have been proposed for effective penetration of nanoparticles deep within the tumor. Together, these various mechanisms of nanoparticle access to tumors highlight the potential of nanotechnology-based tumor-specific targeting.

Self-assembly is one powerful strategy for constructing modular and specific nanosystems with relative synthetic ease.[20,21] We have recently established innovative supramolecular amphiphilic dendrimer nanosystems for tumor imaging,[22-24] exploiting the multivalent cooperativity of dendrimers, the self-assembling of amphiphiles and nanotechnology-based tumor targeting.[25,26] We specifically developed the imaging nanoprobes for effective tumor imaging using single photon emission computed tomography (SPECT) and positron emission tomography (PET).[22-24] In particular, one of these nanoprobes successfully detected tumors which are otherwise undetectable using 2-fluorodeoxyglucose (FDG), the clinical standard for PET imaging of tumors.[22] This exceptional imaging success can be ascribed to the abundance of imaging units conjugated to the dendrimer terminals at the nanoprobe surface, as well as to the EPR-mediated tumor accumulation and targeting.

Motivated by these promising results, we wanted to further expand on the potential applications for self-assembling dendrimer nanosystems by integrating together different imaging agents for multimodality imaging. One frequently used imaging modality is MRI, which provides anatomic, functional, and metabolic information with good spatial resolution and unlimited tissue-penetration.[27,28] While this is particularly beneficial for the detection of deep-seated and small tumors, the MRI signal is not specific and the contrast between tumor and surrounding tissue often needs improving using contrast agents.[29] Nanotechnology-based contrast agents offer the unique advantage of benefiting from passive tumor targeting and deep tumor penetration. This results in high specificity and sensitivity for tumor tissue and minimal biodistribution to healthy tissues, hence improving MRI contrast while minimizing general toxicity.[3,30] Another imaging modality is fluorescence imaging which offers high sensitivity but is limited by tissue penetration depth. Use of near-infrared fluorescence (NIRF) probes

permits real-time imaging and allows the evaluation of tumor margins for intra-operative imaging-guided surgery.[31-33] Multimodality imaging combining MRI and NIRF imaging is expected to harness the advantages of both imaging modalities while overcoming their individual shortcomings, thereby allowing highly sensitive and specific imaging of tumors through the retrieval of complementary information.[34]

Specifically in this study, we aimed to create modular self-assembling dendrimer nanosystems for tumor detection using MRI alone or multimodality imaging combining MRI and NIRF imaging (**Fig. 1A**). Considering that most clinical MRI contrast agents are based on paramagnetic gadolinium (Gd^{3+}), which requires high coordination with water,[35] we conceived the dendrimer nanomicellar system **Gd-1**@ comprising the amphiphilic dendrimer **Gd-1** with Gd^{3+} contrast units at its hydrophilic terminals for MRI (**Fig. 1B**). The aim was to construct a nanosystem offering both the multivalent characteristics of dendrimers and an easy access of water towards Gd^{3+} at the dendrimer surface. To prevent toxicity and stability issues from free Gd^{3+}, the macrocyclic chelator 1,4,7,10-tetraazacyclododecane-1,4,7,10-tetraacetic acid (DOTA) was conjugated at the dendrimer terminals and coordinated with Gd^{3+} to form a Gd-DOTA complex with high thermodynamic and kinetic stability.[29,35]

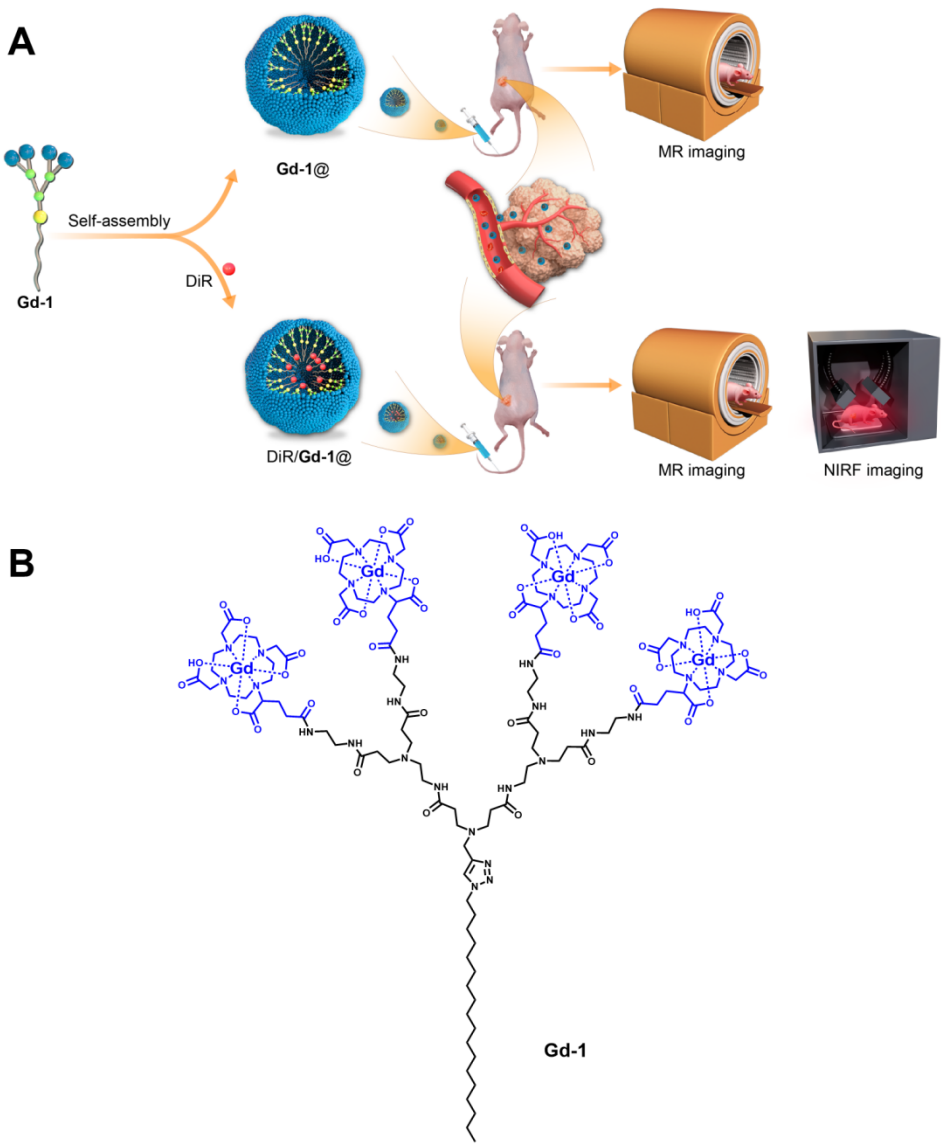

Fig. 1 Self-assembling dendrimer nanosystems for imaging tumors using magnetic resonance and multimodal imaging techniques. (A) Schematic illustration of self-assembling dendrimer nanosystems **Gd-1**@ and DiR/**Gd-1**@ as imaging agents, respectively, for MRI and MR/NIRF bimodality imaging of tumor via EPR effect-based passive tumor targeting. (B) Chemical structure of the amphiphilic dendrimer **Gd-1**.

The unique radiating dendritic structure of the amphiphilic dendrimer **Gd-1** was expected to allow, once self-assembled, the loading of hydrophobic agents in the large void space formed within the inner core of the **Gd-1**@ nanomicelles, as with the loading of drugs for cancer treatment. Considering that NIRF probes are often hydrophobic and insoluble in water, we therefore conceived the dendrimer nanoprobe DiR/**Gd-1**@ formed from the amphiphilic dendrimer **Gd-1** (Fig. 1B) with the hydrophobic NIRF dye DiR loaded within the core of the nanoparticle for bimodality MR/NIRF imaging

(Fig. 1). The Gd^{3+} contrast units at the hydrophilic dendrimer terminals for MRI and the hydrophobic NIRF dye DiR encapsulated within the core for NIRF imaging, ensured the segregation in space of the imaging reporters and prevented their eventual interference during multimodality imaging.

We report here the construction and use of these modular self-assembling nanosystems formed from **Gd-1** for MRI and MR/NIRF bimodality imaging of pancreatic cancer as a proof-of-concept study. Pancreatic cancer is a deadly cancer, difficult to diagnose early on and with, as of yet, no efficacious treatment.[36-38] The most effective treatment for pancreatic cancer is surgical ablation. However for most patients, this is no longer an option due to the lack of effective early detection making their diagnosis of now advanced and metastatic forms too late to allow effective surgical ablation.[39] Therefore, an early detection of pancreatic cancer with a non-invasive imaging modality is of paramount importance. We demonstrate in this study that the nanoprobe **Gd-1**@ enabled cancer detection using MRI with signal enhancement in tumor at a Gd dose 10-fold lower than the conventional dose of the clinical standard Gd-DOTA. In addition, use of the probe DiR/**Gd-1**@ enabled the sensitive detection of pancreatic cancer by MR/NIRF bimodality imaging. These modular supramolecular dendrimer nanosystems offer a new platform for constructing agents that hold great promise for both MRI and MR/NIRF multimodality imaging.

Synthesis of dendrimer Gd-1 and its self-assembly into nanomicelles

The Gd-bearing dendrimer **Gd-1** was synthesized by chelating the dendrimer **1** with Gd^{3+} (Fig. 2A). Specifically, **1** was prepared according to the protocol previously established in our group.[23] Then $GdCl_3$ was added in three portions to the aqueous solution of **1** at 24°C, with the pH of the reaction mixture maintained at 6.5 to ensure optimal acidic conditions for effective chelation between **1** and Gd^{3+}. To address the thermodynamically challenging chelation between Gd^{3+} and the DOTA cage, the reaction mixture was heated to 50°C for 24 h under argon to achieve complete chelation

The resulting crude dendrimer **Gd-1** was purified using dialysis to remove the excess free Gd^{3+}, giving the final product **Gd-1** as a white solid with a yield of up to 92% after lyophilization.

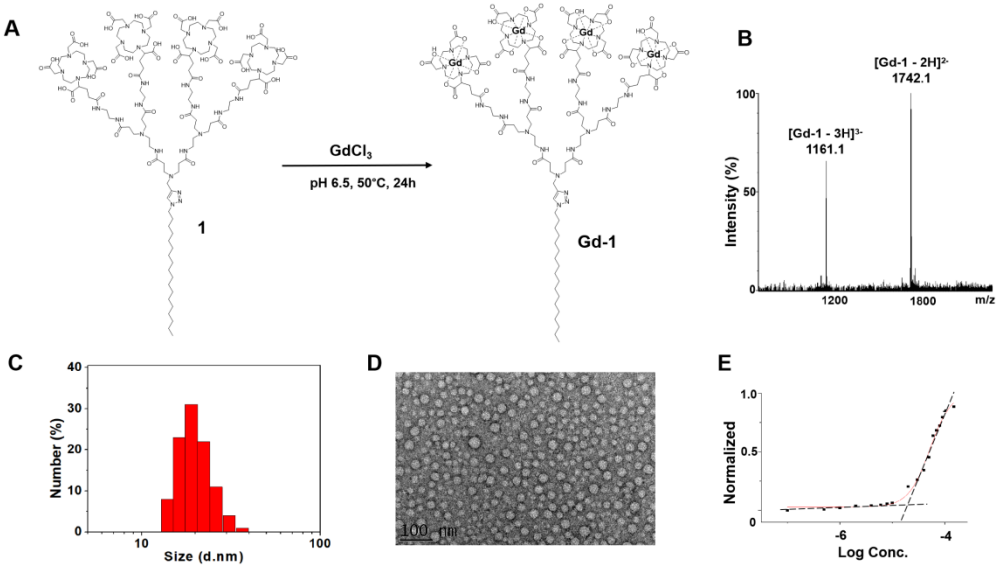

Fig. 2 Synthesis of Gd-1 and its self-assembly into nanomicellar particles Gd-1@. (A) Synthesis scheme and reaction conditions for preparing **Gd-1.** (B) Mass spectroscopic analysis of **Gd-1**. (C) Dynamic light scattering analysis of **Gd-1**@ nanoparticles formed spontaneously by **Gd-1** in H_2O. (D) Transmission electron microscope image of **Gd-1**@ nanoparticles. (E) Evaluation of critical micelle concentration (CMC) of **Gd-1** using fluorescent spectroscopic analysis with Nile red.

Mass spectroscopic analysis confirmed the successful synthesis of **Gd-1**, showing clear-cut peaks for the double-charged [**Gd-1**-2H]$^{2-}$ and triple-charged species [**Gd-1**-3H]$^{3-}$, corresponding to the expected molecular weight of **Gd-1** (Fig. 2B). Additionally, inductively coupled plasma mass spectrometry (ICP-MS) was performed to quantify the content of Gd in **Gd-1**. A Gd content of 17% obtained from ICP-MS agreed with the theoretical value for the chemical structure of **Gd-1**, further supporting the successful chelation of Gd^{3+} in all four DOTA cages.

Gd-1 spontaneously self-assembled in water by virtue of its amphiphilic nature. We first studied the self-assembled nanoparticles **Gd-1**@ using dynamic light scattering (DLS) analysis. The DLS results revealed the formation of small nanoparticles of **Gd-1**@ with a size of approximately 23 ± 1 nm, a typical size for nanomicelles (Fig. 2C).

We further examined **Gd-1**@ using transmission electron microscopy (TEM), and the obtained TEM data confirmed the formation of small, uniform and spherical nanomicelles of **Gd-1**@ with average dimensions of around 21 ± 4 nm (Fig. 2D, Fig. S1), similar to the estimation obtained using DLS (Fig. 2C). It is to note that the optimal size best permitting nanoparticles to exploit the EPR effect for passive tumor targeting and deep tumor penetration is in the range of 12-30 nm. If too small, the nanoparticles will be rapidly removed via renal clearance, but will generate steric hindrance for deep tumor penetration if too big.[40-42] Thus, **Gd-1**@ having a size of ca 20 is particularly interesting for its use in nanotechnology-based bioimaging.

The critical micelle concentration (CMC) of **Gd-1** was then assessed using a fluorescence spectroscopic assay with Nile red. The obtained CMC value of 27 ± 3 μM (Fig. 2E) strongly supports the formation of **Gd-1**@ nanomicelles. The amphiphilic dendrimer **Gd-1** was thus shown to readily and spontaneously self-assemble into small nanomicelles in water.

Advantageous relaxivity with enhanced MRI signals at high magnetic field strength

To explore the potential of **Gd-1**@ as a contrast agent for MRI, it was important to study its ability to decrease the longitudinal T_1 and transverse T_2 relaxation time constants of water media. T_1 shortening by the paramagnetic ion Gd^{3+} results in a signal increase visualized on T_1-weighted MRI as hyperintensities (bright signals), whereas T_2 shortening is associated with signal loss on T_2-weighted MRI.[29] Relaxivity reflects the efficiency of the contrast agent to increase the longitudinal and transverse relaxation rates ($1/T_1$ and $1/T_2$) of water.[29,35] Although Gd-based contrast agents have relatively high longitudinal r_1 relaxivity and generally provide good contrast characteristics at low magnetic field strength, they are often less effective at high magnetic field strengths.[28,35,43] Today however, the demand for MRI scanners operating at high magnetic field strengths ($\geqslant$7 T) is increasing because of the better signal-to-noise ratio

compared to those functioning at lower magnetic field strengths. Considering the tendency of the tissue contrast in T_1-weighted images to decrease with increasing magnetic field strength, we wished to develop efficient contrast agents with good relaxivity at high magnetic field strength to improve imaging quality.

We therefore first assessed the relaxivity of **Gd-1**@ in water using an MRI scanner operating at a magnetic field strength of 11.75T, using the leading contrast agent gadoterate meglumine (Gd-DOTA, also commercially referred to as Dotarem®) as the reference control. By linearly fitting the T_1 relaxation rate ($1/T_1$) against the Gd^{3+} concentration (Fig. 3A), we obtained an r_1 value of 5.9 $s^{-1}mM^{-1}$ (95% confidence interval 5.4 - 6.4) for **Gd-1**@, almost 2-fold higher than that for Gd-DOTA (3.5 $s^{-1}mM^{-1}$, 95% confidence interval 3.4 - 3.6). The enhanced r_1 relaxivity of **Gd-1**@ compared to Gd-DOTA can be ascribed not only to its macromolecular and nanosized structure but also to its strongly hydrophilic and multivalent surface allowing increased interaction of Gd^{3+} ions with water molecules. This constitutes a valuable asset for **Gd-1**@ when used as a T_1 contrast agent in MRI.

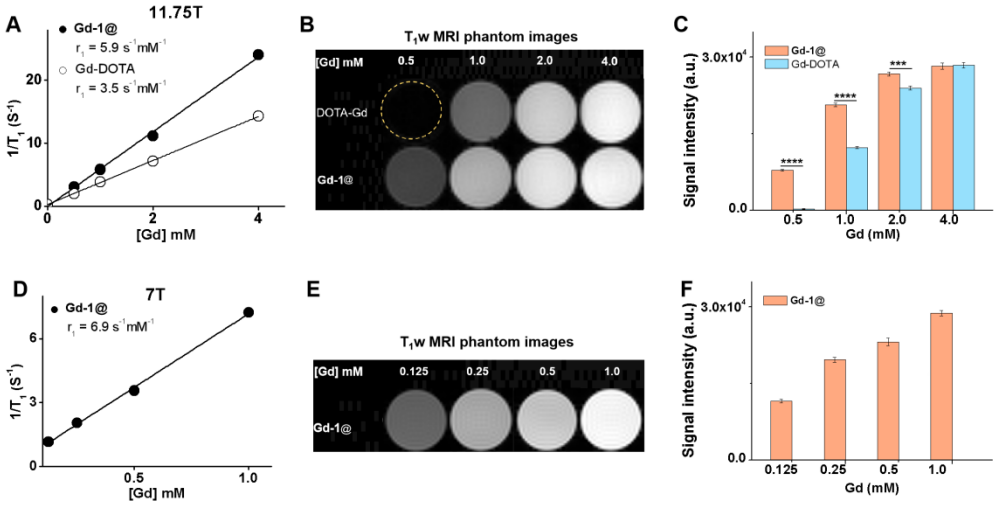

Fig. 3: Favorable relaxivity of the Gd-1@ nanoparticles and enhanced MRI signals at 11.75 T and 7 T. (A) Longitudinal relaxation rate $1/T_1$ of **Gd-1**@ as a function of Gd concentration in water at 11.75T and 20°C. The slope of the linear fit corresponds to relaxivity. The clinical contrast agent Gd-DOTA was used as the reference control. (B) T_1-weighted MRI (T_1w MRI) phantom images and (C) MRI signal intensity of **Gd-1**@ and Gd-DOTA solutions obtained at 11.75T with different Gd concentrations. Data are presented as mean ± SD. The

statistical significance was calculated using two-tailed Student's *t*-test (n = 3, ***P < 0.001, ****P < 0.0001. (D) Longitudinal relaxation rate $1/T_1$ of **Gd-1**@ as a function of Gd concentration in water at 7T and 20°C. The slope of the linear fit corresponds to the relaxivity. (E) T_1w MRI phantom images and (F) MRI signal intensity of **Gd-1**@ solutions obtained at 7T with different Gd concentrations. The coefficients of determination in (A) and (D) are $R^2 > 0.99$.

We next performed phantom studies and acquired T_1-weighted MRI of **Gd-1**@ and Gd-DOTA at different Gd concentrations (Fig. 3B). Both **Gd-1**@ and Gd-DOTA showed an increasing signal intensity with increasing Gd concentrations on T_1-weighted MRI. However, the higher relaxivity of **Gd-1**@ provided brighter MRI signals compared to those from Gd-DOTA at the same Gd concentration (Fig. 3B and C). In particular, at the low Gd concentration of 0.5 mM, at which the Gd-DOTA solution yielded an almost negligible T_1-weighted MRI signal, the signal generated with **Gd-1**@ was over 30-fold stronger (Fig. 3C, Table S1). These results highlight that even at very low Gd concentrations, **Gd-1**@ meets the need for an efficient contrast agent for T_1-weighted MRI at ultra-high magnetic field strength.

We also examined the relaxivity of **Gd-1**@ using an MRI scanner operating at a magnetic field strength of 7T, which is used routinely in preclinical MRI studies but recently also in clinical settings. The r_1 value obtained for **Gd-1**@ at 7T was 6.9 $s^{-1}mM^{-1}$, with a 95% confidence interval of 6.1 – 7.7 (Fig. 3D), which was only slightly higher than that obtained at 11.75T (5.9 $s^{-1}mM^{-1}$). Similarly, T_1-weighted MRI of **Gd-1**@ showed enhanced intensities at increasing Gd concentrations (Fig. 3E/F). Altogether, these data provide evidence supporting the ability of **Gd-1**@ nanoparticles to retain high r_1 relaxivity for T_1-weighted MRI at high magnetic field strengths. The resulting increased magnetic polarization and consequently improved signal is advantageous for detecting smaller lesions.

Excellent safety profile of Gd-1@ nanoparticles

For all bioimaging applications, the safety of the imaging agents is an important consideration. Some Gd-based contrast agents have been reported to cause severe side effects such as nephrogenic systemic fibrosis in patients with renal failure.[44,45] It was therefore necessary to assess the safety profile of **Gd-1**@ prior to in vivo bioimaging studies.

We first examined the metabolic cytotoxicity of **Gd-1**@ on various cells using the PrestoBlue cell viability assay. At Gd concentrations up to 2000 μM, **Gd-1**@ exhibited no notable cytotoxicity on different cell lines including human kidney cells (HEK293), Madin-Darby canine kidney cells (MDCK), alpha mouse liver 12 cells (AML12), and murine fibroblast cells (L929) (Fig. 4A). These results support the high potential of **Gd-1**@ in biomedical studies.

We also evaluated the effect of **Gd-1**@ on cell membrane integrity using the lactate dehydrogenase (LDH) assay for which LDH release signals plasma membrane damage. The lack of obvious LDH release for any of the tested cell lines at Gd concentrations ranging from 15.6 μM to 2000 μM (Fig. 4B) demonstrated the biocompatibility of **Gd-1**@ for further application.

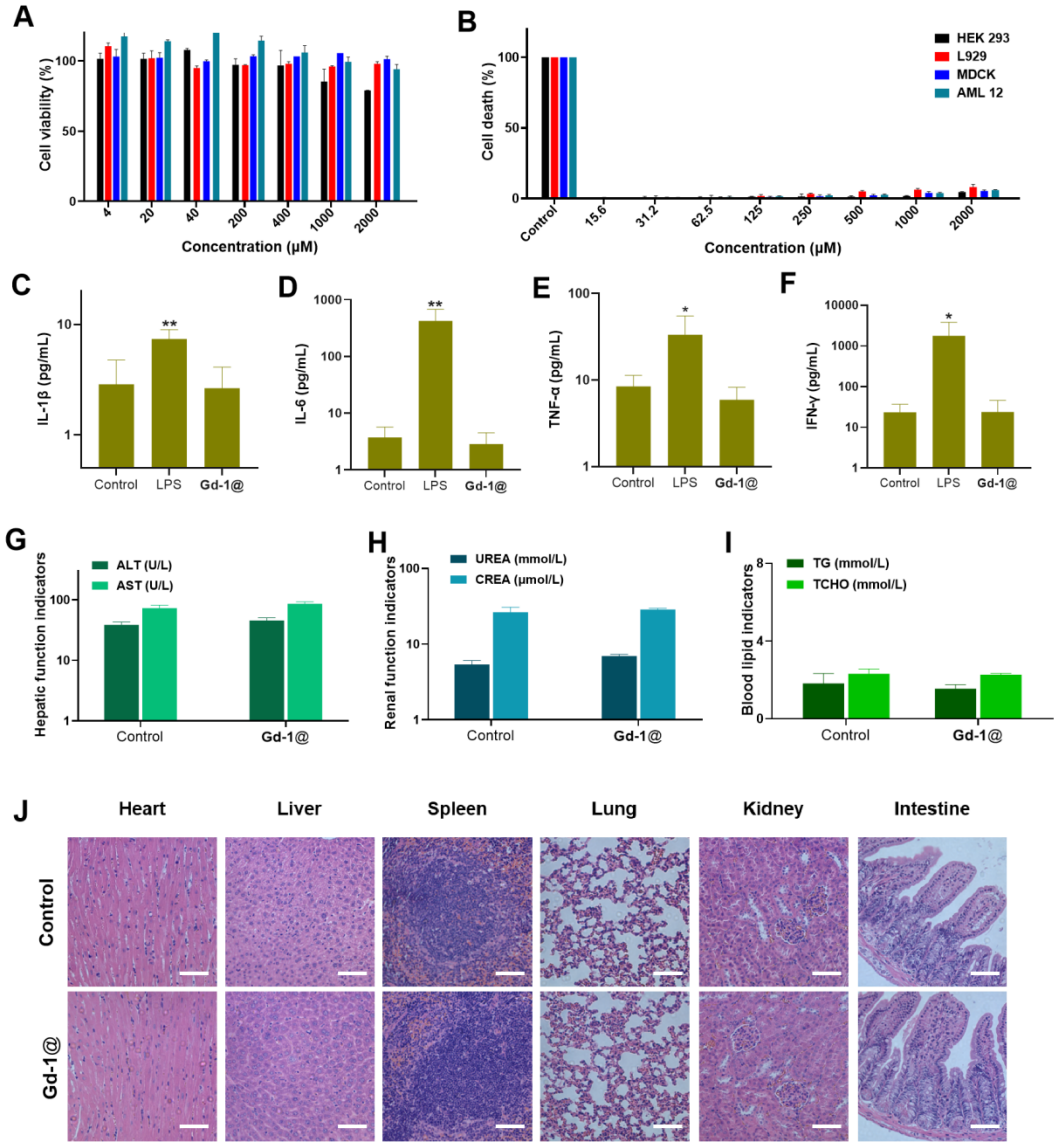

Fig. 4: Safety evaluation of Gd-1@. (A) Toxicity evaluation of **Gd-1**@ on HEK293, MDCK, AML12, and L929 cells in a Gd^{3+} concentration range of 4 to 2000 μM at 48 h post-treatment using the PrestoBlue assay. (B) Evaluation of membrane damage by **Gd-1**@ on HEK293, MDCK, AML12, and L929 cells in a Gd^{3+} concentration range of 15.6 to 2000 μM using LDH assay. Lysis buffer provided in the commercial LDH assay kit was used as a positive control (Control). (C-J) In vivo toxicity evaluation of **Gd-1**@ in healthy mice (n = 4 for each group of mice). Quantification of the major inflammatory cytokines in serum (C) IL-1β, (D) IL-6, (E) TNF-α, and (F) INF-γ. Data are presented as mean ± SD (n = 4). The statistical significance was analyzed by one-way ANOVA with a Tukey's multiple comparison test (ns not significant, *P < 0.05, **P < 0.01). Assessment of liver and kidney function and of blood lipids by quantifying the levels of biomarkers (G) alanine aminotransferase (ALT) and aspartate aminotransferase (AST), (H) urea and creatinine, (I) triglycerides and total cholesterol in serum. (J) Histological analysis of tissues from major organs using hematoxylin and eosin staining. Mice received either **Gd-1**@ (22.0 mg/kg, iv injection) or normal saline (control, iv injection). Scale bar, 200 μm.

We next assessed inflammatory response to **Gd-1**@, as well as blood biochemistry and pathology in major organs of healthy mice. While mice in the positive control group treated with lipopolysaccharide (LPS) showed significantly increased levels of the inflammatory factors IL-1β, IL-6, TNF-α, and INF-γ (Fig. 4C-F), those treated with **Gd-1**@ exhibited inflammatory cytokine levels similar to those found in the negative control group of mice treated with normal saline. These results indicate that **Gd-1**@ induces no inflammatory reactions. Additionally, the liver function indicators alanine aminotransferase (ALT) and aspartate aminotransferase (AST) (Fig. 4G), and the kidney function indicators urea and creatinine (Fig. 4H), confirmed no functional injury of liver or kidney. The lack of difference in the levels of the blood lipid markers cholesterol and triglycerides between the **Gd-1**@ treatment group and the saline control group (Fig. 4I) further emphasized the biocompatibility of **Gd-1**@. Additional histochemical analysis of main organs using hematoxylin and eosin staining, revealed that mice treated with **Gd-1**@ showed normal cell morphology with regularly arranged cells comparable to those found in the control group treated with saline (Fig. 4J). This indicates no pathological effect upon treatment with **Gd-1**@ and, together with the in vitro data above, demonstrates that **Gd-1**@ has a satisfactory safety profile for further in vivo bioimaging studies.

In vivo MRI of tumors at high magnetic field strength

Motivated by the excellent safety profile and promising relaxivity properties of **Gd-1**@, we performed in vivo MRI experiments in a tumor xenograft model generated with primary pancreatic cancer L-IPC cells from a human patient.[22,46] Considering the almost 2-fold higher relaxivity of **Gd-1**@ compared with the clinical agent Gd-DOTA at 11.75 T, we injected **Gd-1**@ at a dose of 0.05 mmol Gd/kg, corresponding to half of the typical clinical dose (0.10 mmol Gd/kg) of Gd-DOTA. We acquired T_1-weighted MRI of the tumor (Fig. 5A) and the liver (Fig. 5C) before and at 4 h, 24 h and 48 h post-injection of **Gd-1**@ in order to monitor the enhancement of the MRI signals. All these experiments were performed at the ultra-high magnetic field of 11.75T.

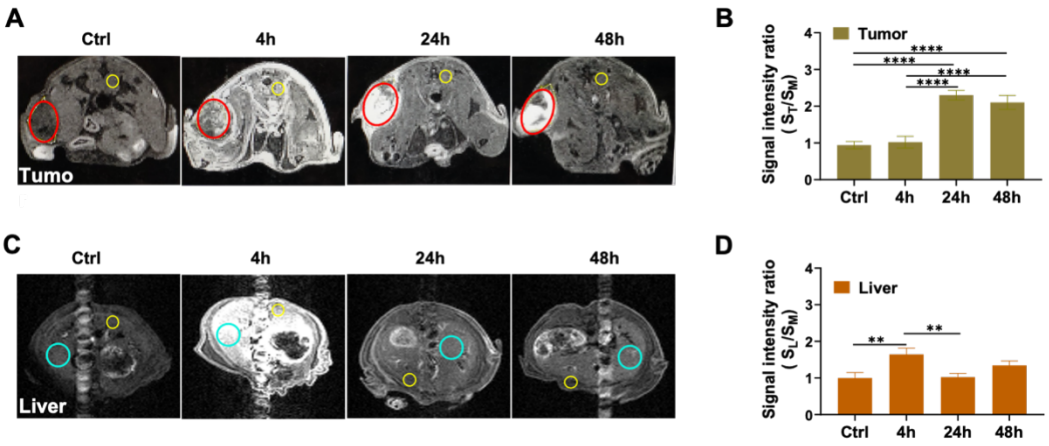

Fig. 5: *In vivo* MRI of tumor and liver using Gd-1@ at ultra-high magnetic field (11.75T). Transverse MRI of mice bearing L-IPC pancreatic tumor before (control, CTRL) and 4h, 24h and 48h after iv injection of **Gd-1** (dose of 0.05 mmol Gd/kg), (n = 3 for each group of mice). The MR images show uptake of **Gd-1**@ in (A) subcutaneous tumor (red oval) and (C) liver (cyan circle) in the same mouse. A flow artifact (produced by the phase encoding) from the aorta is visible in the abdominal MRI (C) but was avoided when drawing the region of interest (ROI) for liver signal analysis. Changes in signal intensity ratios of (B) tumor and (D) liver after **Gd-1**@ injection. Paravertebral muscles were used for normalization and highlighted with yellow circles. Data are presented as the mean ± SD (n = 3). The statistical significance was calculated using ANOVA with Tukey's multiple comparison test (**P < 0.01, ****P < 0.0001).

As shown in Fig. 5A/C, strong MRI signals were observed throughout the body of the tested mice with intense enhancement in the liver at 4 h post-injection of **Gd-1**@. However, at 24 h and 48 h post-injection, while the MRI signals drastically decreased in the liver and normal tissues (Fig. 5C/D), they were significantly enhanced in the tumor (Fig. 5A/B). These results indicate the clearance of **Gd-1**@ from liver and normal tissues, and its specific accumulation in tumor that permits the sensitive and specific tumor detection and imaging. We attribute this tumor-specific enrichment of **Gd-1**@ to the EPR effect of the tumor microenvironment harboring leaky vasculature and dysfunctional lymphatic drainage. This phenomenon allows passive tumor targeting by promoting the accumulation and retention of nanosized imaging agents within the tumor lesion rather than normal tissue, hence enabling effective tumor imaging and detection. It is also to note that pancreatic cancer cells show enhanced macropinocytosis activity[47,48] which, alongside the EPR effect, likely contributes towards the significant

uptake and accumulation of **Gd-1**@ within the tumor lesion thus promoting effective and specific tumor imaging.

Importantly, the T_1-weighted MRI signals in the liver were very weak at 24 h and 48 h post-injection, reaching intensity levels similar to those recorded prior to **Gd-1**@ injection (Fig. 5C/D). These data support the rapid clearance of **Gd-1**@ from the liver and excretion in urine, thus avoiding any eventual toxicity associated with retention in healthy tissues. We also note that no mice treated with **Gd-1**@ showed any abnormal behavior at any point, or any notable weight loss during the experimental period. These results correlate well with those obtained for the safety assay of **Gd-1**@ in healthy mice (Fig. 4).

Multimodal MR/NIRF imaging

Encouraged by the excellent results obtained with **Gd-1**@ for tumor imaging using MRI, we next constructed the nanoprobe DiR/**Gd-1**@ for multimodality MR/NIRF imaging. We did this by encapsulating the NIRF dye DiR within the nanomicelles formed by **Gd-1,** reaching an encapsulation yield of up to 99% using the film-dispersion method.[49] The DiR/**Gd-1**@ nanoparticles retained the characteristic excitation and emission spectra of DiR in the near-infrared range (Fig. 6A), similar to that shown by free DiR dye dissolved in organic solvent (Fig. S2). This fluorescence spectroscopic feature is an important prerequisite for use of DiR/**Gd-1**@ in NIRF imaging.

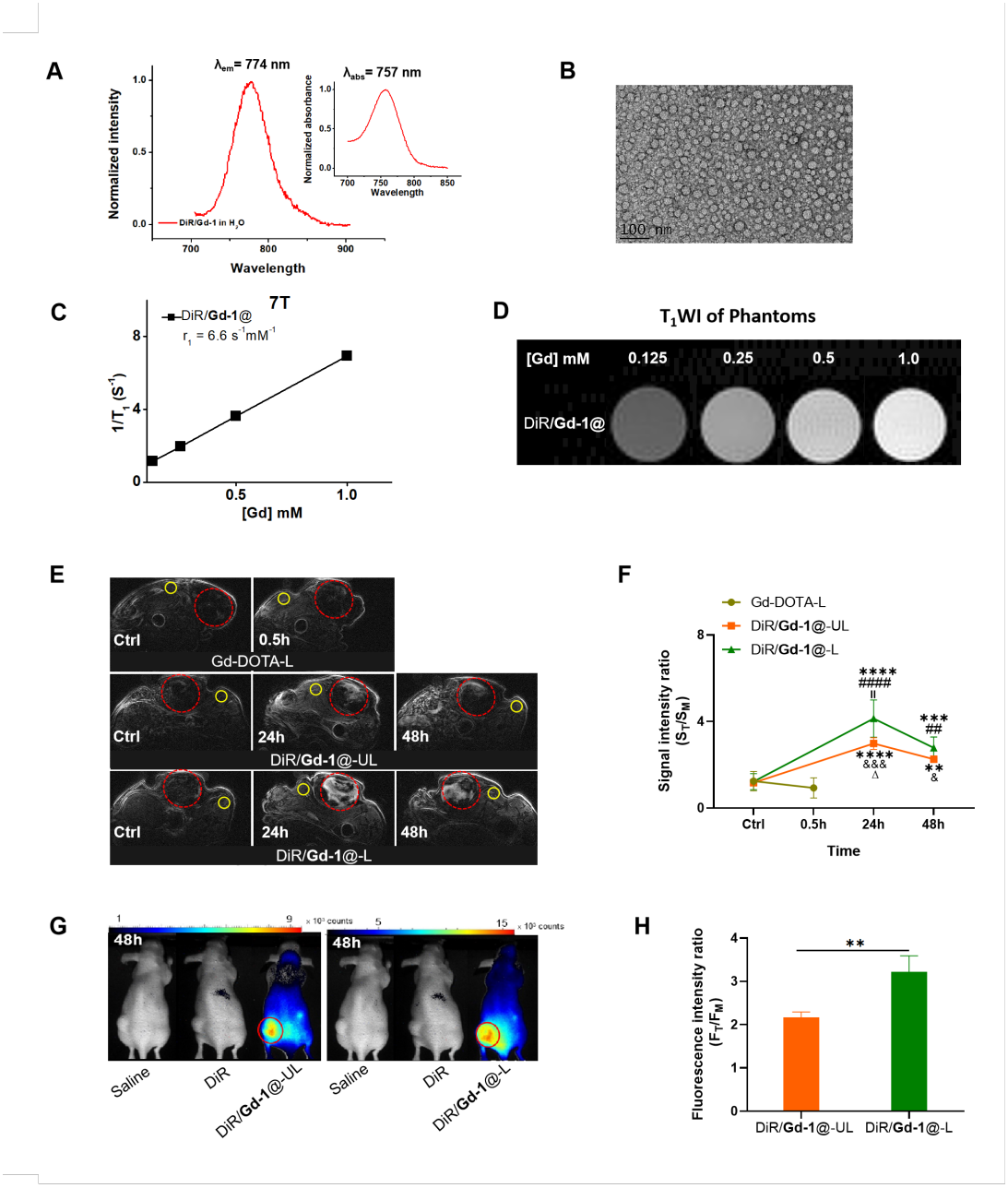

Fig. 6 DiR/Gd-1@ for MR/NIRF dual imaging of tumor. (A) Normalized absorbance and emission spectra of DiR/**Gd-1**@ in H_2O. (B) Transmission electron microscope imaging of DiR/**Gd-1**@. (C) Longitudinal relaxation rate $1/T_1$ for DiR/**Gd-1**@ as a function of Gd concentration. The slope of the linear fit with $R^2 > 0.99$ corresponds to the relaxivity of the contrast agent in water at 7T and 20°C. (D) T_1-weighted MRI of solutions of DiR/**Gd-1**@ at different Gd concentrations. (E–H) Multimodal MR/NIRF imaging of the L-IPC-xenograft mice before (control, ctrl) and after iv injection of DiR/**Gd-1**@ (n = 3 for each group of mice). (E) Transverse T_1-weighted MRI acquired at 7T of tumors in L-IPC xenograft mice injected with Gd-DOTA at a low dose (Gd-DOTA-L, 0.025 mmol Gd/kg; upper panel), DiR/**Gd-1**@ at an ultra-low dose (DiR/**Gd-1**@-UL, 0.01 mmol Gd/kg, 27 μg DiR/kg; middle panel) and DiR/**Gd-1**@ at a low dose (DiR/**Gd-1**@-L, 0.025 mmol Gd/kg, 67 μg DiR/kg; lower panel) at different time points after injection. Red dashed circles indicate the tumor location, yellow

circles indicate the thigh muscle region used for signal normalization. (F) Signal intensity ratio of tumor to adjacent muscles obtained from MRI data. Data denote mean ± SD (n = 3). The statistical significance was calculated by two-way ANOVA with a Tukey's multiple comparison test. **P < 0.01, ***P < 0.001, ****P < 0.0001 versus Gd-DOTA 0.5h group; $^{\#\#}$P < 0.01,$^{\#\#\#\#}$P < 0.0001 versus DiR/Gd-1@-L Ctrl group; $^{\&}$P < 0.05, $^{\&\&\&}$P < 0.001 versus DiR/Gd-1@-UL Ctrl group; $^{\Delta}$P < 0.05 versus DiR/Gd-1@-UL48h group; ^{II}P < 0.01 versus DiR/Gd-1@-L48h group. (G) NIRF images after in vivo MRI at 48 h post-injection. (H) Fluorescence intensity ratio of tumor to adjacent muscle obtained from NIRF imaging data. Red circles indicate the tumor locations. Data denote mean ± SD (n = 3). The statistical significance was calculated by two-tailed Student's t test for comparison between two groups. **P < 0.01.

Remarkably, the DiR/**Gd-1**@ nanoparticles were small and uniform in shape, similar to, though slightly smaller (19–20 nm) (Fig. 6B, Fig. S3) than, **Gd-1**@ (21–23 nm). This difference in size might be ascribed to the hydrophobic DiR loaded within the nanomicellar core, which enabled the assembly of more compact DiR/**Gd-1**@ nanoparticles via the enhanced interaction between DiR and the hydrophobic chain in dendrimer. The resulting smaller nanosize would be expected to be beneficial, by facilitating extravasation and deep penetration into tumor parenchyma, thus enabling more efficient EPR-based accumulation in tumors[22,40,49].

We next investigated whether encapsulation of DiR had an impact on the MRI properties of the Gd/DOTA terminals on the surface of DiR/**Gd-1**@. DiR/**Gd-1**@ and **Gd-1**@ showed no statistical difference in terms of r_1 relaxivities at 7T (Fig. 6C), respectively 6.6 $s^{-1}mM^{-1}$ (95% confidence interval, 6.5 – 6.7) and 6.9 $s^{-1}mM^{-1}$ (Fig. S4A). Consequently, T_1-weighted MR images from DiR/**Gd-1**@ solutions at different concentrations **(**Fig. 6D) provided similar signal intensities to those of **Gd-1**@ solutions (Fig. S4B). These results indicate that encapsulation of DiR has no obvious effect on the access of water protons to DiR/**Gd-1**@, which thus maintains good relaxivity. This can be reasonably explained by the DiR molecules being encapsulated within the interior hydrophobic core and thereby sufficiently segregated in space in relation to the Gd/DOTA entities located on the surface of the DiR/**Gd-1**@.

Importantly, DiR/**Gd-1**@ was devoid of any notable toxicity. Indeed, at concentrations up to 1.0 mM, it caused no metabolic cytotoxicity or membrane damage (Fig. S5A/B). The *in vivo* safety evaluation performed using healthy mice also revealed no alteration of the major blood biochemical markers (alanine transaminase, aspartate transaminase, urea, creatinine, triacylglycerol, and total cholesterol) (Fig. S5C-S5E), indicating that liver and kidney functioned well with good biocompatibility following administration of DiR/**Gd-1**@. In addition, histological analysis of the main organs showed no pathological changes (Fig. S5F). The lack of cytotoxic effects and acute toxicity highlights a good and reliable safety profile for DiR/**Gd-1**@, similar to **Gd-1**@.

Encouraged by the excellent safety profile and MRI properties and performance shown by **Gd-1**@ at a dose of 0.05 mmol Gd/kg in the above-mentioned MRI studies, we wished to further reduce the Gd dose for the MR/NIRF bimodality imaging. We used DiR/**Gd-1**@ at the low dose of 0.025 mmol Gd/kg and an ultra-low dose of 0.010 mmol Gd/kg **(**Fig. 6E), corresponding respectively to 1/4 and 1/10 of the clinically recommended dose (0.10 mmol Gd/kg). As in the above-mentioned experiments, we used the patient-derived pancreatic cancer L-IPC xenograft model and the clinical contrast agent Gd-DOTA as the control for in vivo MRI studies. Gd-DOTA is a non-specific low molecular weight contrast agent with a short circulation time and a blood half-life of less than 30 minutes in mice. As expected therefore, we observed no MRI signal enhancement in tumors 30 minutes post-injection when compared with the images acquired prior to injection using the MRI scanner operating at the magnetic field strength of 7T **(**Fig. 6E, upper panel). These results agree with those reported in the literature, and confirm the lack of retention of Gd-DOTA within the tumor lesion and its rapid elimination from the body.[50]

In contrast, DiR/**Gd-1**@ at doses of 0.010 and 0.025 mmol Gd/kg displayed contrast enhancement at 24 h and 48 h post-injection **(**Fig. 6E, middle and lower panels**)**. Notably, at the tumor site, the signal intensity at 24 h was significantly higher than at

48 h post-injection, which can be ascribed to a maximum tumor uptake of DiR/**Gd-1**@ at 24 h post-injection and subsequent gradual elimination over time. The MRI sensitivity for tumor detection was quantified as the difference in signal intensity between the tumor and adjacent normal muscle tissues. As shown in Fig. 6F, the contrast enhancement at both 24h and 48h was significant with respect to the pre-injection timepoint. The much-reduced Gd-dose and the longer persistence within the tumor observed with **Gd-1**@, alongside an effective contrast enhancement are particularly advantageous, as it allows preventing eventual Gd-related toxicity and permitting a longer observation period if necessary (at least 48 hours after injection).

At 48 h post-injection, the same mice used for the in vivo MRI experiments were then subjected to NIRF imaging to generate matched sets of dual modality imaging data. We observed strong fluorescence signals at the tumor sites in mice treated with DiR/**Gd-1**@ but no signal at all in the control mice treated with saline or small molecular DiR dye alone (Fig. 6G). The results of the NIRF imaging of tumors with DiR/**Gd-1**@ concord well with those obtained using MRI. In addition, the NIRF signals in the tumor were 2–3-fold stronger than those of nearby tissues (Fig. 6H). The signal hyperintensities in tumor tissue shown on both MRI and NIRF imaging confirm that DiR/**Gd-1**@ is a promising nanoprobe for sensitive and specific MR/NIRF dual-modality tumor imaging.

Conclusions

In this study, we developed modular dendrimer nanoprobes for MRI and MR/NIRF bimodality imaging, respectively. These nanoprobes were constructed through self-assembly of the amphiphilic dendrimer **Gd-1**, which is composed of a long hydrophobic alkyl chain and a small hydrophilic poly(amidoamine) dendron bearing four Gd^{3+} ions chelated within the DOTA rings at the terminals. By virtue of their small nanosize and abundance of multivalent terminals, the nanoprobes **Gd-1**@ and DiR/**Gd-1**@ showed high levels of accumulation in tumor tissue and higher r_1 relaxivity than the clinical

standard Gd-DOTA. This resulted in excellent tumor imaging contrast at low Gd-doses down to 1/10th of the standard clinical dose of Gd-DOTA. Additionally, the DiR/**Gd-1**@ probe harbored the NIRF dye DiR within its core for NIRF imaging. The localization of this fluorescence dye at the core meant that it was sufficiently segregated in space away from the Gd/DOTA terminals to avoid any impact on the relaxivity, thereby providing sensitive MR and NIRF imaging of the tumor.

In this proof-of-concept study, the self-assembling dendrimer nanosystems provided not only enhanced imaging contrast for both MRI and NIRF imaging but also effective imaging at much lower Gd doses compared to the clinically used dose. This is an important advantage as it permits the prevention of eventual Gd^{3+}-related toxicity. The other advantage of **Gd-1**@ or DiR/**Gd-1**@ in comparison to clinically approved agents is their long half-lives within tumor tissue, likely due to the EPR effect and enhanced macropinocytosis activity found in the tumor microenvironment. This prolonged steady-state concentration within tumor tissue permits high resolution imaging in cases where a long observation time is required. The capacity to acquire images with increased spatial resolution and contrast also increases the chance of detecting small lesions for early diagnosis. Consequently, the DiR/**Gd-1**@ probe shows great promise for use in MRI and MR/NIRF dual imaging and offers the potential for improved imaging efficacy at very low doses for the early detection of pancreatic cancer, an unmet medical need. Further studies dedicated to detailed pharmacokinetic investigation, long-term safety evaluation and robust validation in different tumor models are required for the translation of these nanosystems into real life applications.

Since the first MRI study on dendrimer-based contrast agents by Lauterbur in 1994,[51] dendrimers have been considered and appreciated as valuable molecular marvels for bioimaging by virtue of their unique precise structure, geometrical symmetry and cooperative multivalency.[22,30,52,53] This study has demonstrated the potential of self-assembling dendrimer nanosystems for constructing modular and effective contrast agents not only for MRI but also for MR/NIRF multimodality imaging. Such self-assembling dendrimer nanosystems can be applied to other

multimodality imaging as well as to theranostics. Notably, multimodality imaging combines complementary information from different imaging systems, thereby compensating for each of their weaknesses to provide more complete imaging data for precision medicine. The current study offers a promising nanotechnology platform based on modular and self-assembling dendrimer material for the creation of multimodality imaging agents for biomedical applications.

Experimental Section

In Vivo Imaging Study: all experimental procedures on animals were approved by the Animal Ethics Committee of Marseille Number 14 (N°: 2019042518563696, 2019040115419686). All mice were housed in specific pathogen-free conditions according to current European regulations. Female and male NMRI-Foxn1nu/Foxn1nu mice (nude mice) were provided by Janvier Laboratories. Mice were housed in environmentally-enriched cages placed in a temperature- and hygrometry-controlled room with daily monitoring, and were fed *ad libitum* with free access to water. A full description of the materials and methods as well as all experimental details is provided in the Supporting Information.

In Vivo Toxicity Evaluation: all procedures were approved by the Institutional Animal Care and Use Committee of China Pharmaceutical University and were performed in accordance with their guidelines and policies. The approval numbers are "2021-11-020" and "23-10-009". Male CD-1 mice (6-week-old) were purchased from Sino-British SIPPR/BK Lab Animal Ltd (Shanghai, China). All mice involved in this work were kept at the Animal Center of China Pharmaceutical University Laboratory and received the required animal care and monitoring. A full description of the materials and methods as well as all experimental details is provided in the Supporting Information.

Author contributions

LP conceived and coordinated the project; LD, ZL, AYTH and TR synthesized the agents; LD, ZL, SG and TAPB performed the characterization; JI provided the animal model; LD, YJ and BL performed the animal experiments; LD, BL and CG assessed toxicity; TAPB, AV, LD and YJ performed in vivo imaging experiments; LD, ZL, AYTH, C-LK, XL, TAPB, AV, MB and LP analyzed the data; LD, TAPB, AV, XL, MB and LP wrote the paper. All authors proof-read the manuscript.

Acknowledgements

This work was supported by the Ligue Nationale Contre le Cancer (EL2016, EL2021 LNCCLiP, LP; doctoral fellowship grant, ZL), China Scholarship Council (LD), the French National Research Agency under the framework of the ERA-NET EURONANOMED European Research project 'NAN-4-TUM' (LP), the EU H2020 Research and Innovation program NMBP "SAFE-N-MEDTECH" (2019-2023) (grant agreement No. 814607, LP, TR), Fondation Recherche Médicale (YJ) and National Key Research & Development Program of China for International S&T Cooperation Projects (2018YFE0117800) (XL). The relaxometric and preclinical MRI studies were performed at CRMBM, which is a member of France Life Imaging (grant ANR-11-INBS-0006 from the French "Investissements d'Avenir" program).

References:

(1) James, M. L.; Gambhir, S. S. A Molecular Imaging Primer: Modalities, Imaging Agents, and Applications. *Physiological Reviews* **2012**, *92*, 897-965.

(2) Believing in seeing. *Nature Materials* **2014**, *13*, 99-99.

(3) Smith, B. R.; Gambhir, S. S. Nanomaterials for In Vivo Imaging. *Chemical Reviews* **2017**, *117*, 901-986.

(4) Chen, H.; Zhang, W.; Zhu, G.; Xie, J.; Chen, X. Rethinking cancer nanotheranostics. *Nature Reviews Materials* **2017**, *2*, 17024.

(5) Matsumura, Y.; Maeda, H. A new concept for macromolecular therapeutics in cancer chemotherapy: mechanism of tumoritropic accumulation of proteins and the antitumor agent smancs. *Cancer Res* **1986**, *46*, 6387-6392.

(6) Gerlowski, L. E.; Jain, R. K. Microvascular permeability of normal and neoplastic tissues. *Microvascular Research* **1986**, *31*, 288-305.

(7) Maeda, H.; Wu, J.; Sawa, T.; Matsumura, Y.; Hori, K. Tumor vascular permeability and the EPR effect in macromolecular therapeutics: a review. *J Control Release* **2000**, *65*, 271-284.

(8) Maeda, H. Toward a full understanding of the EPR effect in primary and metastatic tumors as well as issues related to its heterogeneity. *Adv Drug Deliv Rev* **2015**, *91*, 3-6.

(9) Shi, Y.; van der Meel, R.; Chen, X.; Lammers, T. The EPR effect and beyond: Strategies to improve tumor targeting and cancer nanomedicine treatment efficacy. *Theranostics* **2020**, *10*, 7921-7924.

(10) Sun, R.; Xiang, J.; Zhou, Q.; Piao, Y.; Tang, J.; Shao, S.; Zhou, Z.; Bae, Y. H.; Shen, Y. The tumor EPR effect for cancer drug delivery: Current status, limitations, and alternatives. *Advanced Drug Delivery Reviews* **2022**, *191*, 114614.

(11) Petersen, G. H.; Alzghari, S. K.; Chee, W.; Sankari, S. S.; La-Beck, N. M. Meta-analysis of clinical and preclinical studies comparing the anticancer efficacy of liposomal versus conventional non-liposomal doxorubicin. *J Control Release* **2016**, *232*, 255-264.

(12) Nel, A.; Ruoslahti, E.; Meng, H. New Insights into "Permeability" as in the Enhanced Permeability and Retention Effect of Cancer Nanotherapeutics. *ACS Nano* **2017**, *11*, 9567-9569.

(13) de Lázaro, I.; Mooney, D. J. A nanoparticle's pathway into tumours. *Nature Materials* **2020**, *19*, 486-487.

(14) Matsumoto, Y.; Nichols, J. W.; Toh, K.; Nomoto, T.; Cabral, H.; Miura, Y.; Christie, R. J.; Yamada, N.; Ogura, T.; Kano, M. R.; Matsumura, Y.; Nishiyama, N.; Yamasoba, T.; Bae, Y. H.; Kataoka, K. Vascular bursts enhance permeability of tumour blood vessels and improve nanoparticle delivery. *Nature Nanotechnology* **2016**, *11*, 533-538.

(15) Tee, J. K.; Yip, L. X.; Tan, E. S.; Santitewagun, S.; Prasath, A.; Ke, P. C.; Ho, H. K.; Leong, D. T. Nanoparticles' interactions with vasculature in diseases. *Chem Soc Rev* **2019**, *48*, 5381-5407.

(16) Sindhwani, S.; Syed, A. M.; Ngai, J.; Kingston, B. R.; Maiorino, L.; Rothschild, J.; MacMillan, P.; Zhang, Y.; Rajesh, N. U.; Hoang, T.; Wu, J. L. Y.; Wilhelm, S.; Zilman, A.; Gadde, S.; Sulaiman, A.; Ouyang, B.; Lin, Z.; Wang, L.; Egeblad, M.; Chan, W. C. W. The entry of nanoparticles into solid tumours. *Nature Materials* **2020**, *19*, 566-575.

(17) Chen, S.; Zhong, Y.; Fan, W.; Xiang, J.; Wang, G.; Zhou, Q.; Wang, J.; Geng, Y.; Sun, R.; Zhang, Z.; Piao, Y.; Wang, J.; Zhuo, J.; Cong, H.; Jiang, H.; Ling, J.; Li, Z.; Yang, D.; Yao, X.; Xu, X.; Zhou, Z.; Tang, J.; Shen, Y. Enhanced tumour penetration and prolonged circulation in blood of polyzwitterion-drug conjugates with cell-membrane affinity. *Nat Biomed Eng* **2021**, *5*, 1019-1037.

(18) Wu, X.; Tang, T.; Wei, Y.; Cummins, K. A.; Wood, D. K.; Pang, H.-B. Extracellular Vesicles Mediate the Intercellular Exchange of Nanoparticles. *Advanced Science* **2022**, *9*, 2102441.

(19) Jiang, Y.; Lyu, Z.; Ralahy, B.; Liu, J.; Roussel, T.; Ding, L.; Tang, J.; Kosta, A.; Giorgio, S.; Tomasini, R.; Liang, X.-J.; Dusetti, N.; Iovanna, J.; Peng, L. Dendrimer nanosystems for adaptive tumor-assisted drug delivery via extracellular vesicle hijacking. *Proceedings of the National Academy of Sciences* **2023**, *120*, e2215308120.

(20) Lehn, J.-M. Toward Self-Organization and Complex Matter. *Science* **2002**, *295*, 2400-2403.

(21) Mendes, A. C.; Baran, E. T.; Reis, R. L.; Azevedo, H. S. Self-assembly in nature: using the principles of nature to create complex nanobiomaterials. *Wiley Interdiscip Rev Nanomed Nanobiotechnol* **2013**, *5*, 582-612.

(22) Garrigue, P.; Tang, J.; Ding, L.; Bouhlel, A.; Tintaru, A.; Laurini, E.; Huang, Y.; Lyu, Z.; Zhang, M.; Fernandez, S.; Balasse, L.; Lan, W.; Mas, E.; Marson, D.; Weng, Y.; Liu, X.; Giorgio, S.; Iovanna, J.; Pricl, S.; Guillet, B.; Peng, L. Self-assembling supramolecular dendrimer nanosystem for PET imaging of tumors. *Proceedings of the National Academy of Sciences* **2018**, *115*, 11454-11459.

(23) Ding, L.; Lyu, Z.; Tintaru, A.; Laurini, E.; Marson, D.; Louis, B.; Bouhlel, A.; Balasse, L.; Fernandez, S.; Garrigue, P.; Mas, E.; Giorgio, S.; Pricl, S.; Guillet, B.; Peng, L. A self-assembling amphiphilic dendrimer nanotracer for SPECT imaging. *Chemical Communications* **2020**, *56*, 301-304.

(24) Ding, L.; Lyu, Z.; Louis, B.; Tintaru, A.; Laurini, E.; Marson, D.; Zhang, M.; Shao, W.; Jiang, Y.; Bouhlel, A.; Balasse, L.; Garrigue, P.; Mas, E.; Giorgio, S.; Iovanna, J.; Huang, Y.; Pricl, S.; Guillet, B.; Peng, L. Surface Charge of Supramolecular Nanosystems for In Vivo Biodistribution: A MicroSPECT/CT Imaging Study. *Small* **2020**, *16*, 2003290.

(25) Chen, J.; Zhu, D.; Liu, X.; Peng, L. Amphiphilic Dendrimer Vectors for RNA Delivery: State-of-the-Art and Future Perspective. *Accounts of Materials Research* **2022**, *3*, 484-497.

(26) Lyu, Z.; Ding, L.; Tintaru, A.; Peng, L. Self-Assembling Supramolecular Dendrimers for Biomedical Applications: Lessons Learned from Poly(amidoamine) Dendrimers. *Accounts of Chemical Research* **2020**, *53*, 2936-2949.

(27) Harisinghani, M. G.; O'Shea, A.; Weissleder, R. Advances in clinical MRI technology. *Science Translational Medicine* **2019**, *11*, eaba2591.

(28) Terreno, E.; Castelli, D. D.; Viale, A.; Aime, S. Challenges for Molecular Magnetic Resonance Imaging. *Chemical Reviews* **2010**, *110*, 3019-3042.

(29) Wahsner, J.; Gale, E. M.; Rodríguez-Rodríguez, A.; Caravan, P. Chemistry of MRI Contrast Agents: Current Challenges and New Frontiers. *Chemical Reviews* **2019**, *119*, 957-1057.

(30) Villaraza, A. J. L.; Bumb, A.; Brechbiel, M. W. Macromolecules, Dendrimers, and Nanomaterials in Magnetic Resonance Imaging: The Interplay between Size, Function, and Pharmacokinetics. *Chemical Reviews* **2010**, *110*, 2921-2959.

(31) Wang, K.; Du, Y.; Zhang, Z.; He, K.; Cheng, Z.; Yin, L.; Dong, D.; Li, C.; Li, W.; Hu, Z.; Zhang, C.; Hui, H.; Chi, C.; Tian, J. Fluorescence image-guided tumour surgery. *Nature Reviews Bioengineering* **2023**, *1*, 161-179.

(32) Hong, G.; Antaris, A. L.; Dai, H. Near-infrared fluorophores for biomedical imaging. *Nature Biomedical Engineering* **2017**, *1*, 0010.

(33) Hu, Z.; Fang, C.; Li, B.; Zhang, Z.; Cao, C.; Cai, M.; Su, S.; Sun, X.; Shi, X.; Li, C.; Zhou, T.; Zhang, Y.; Chi, C.; He, P.; Xia, X.; Chen, Y.; Gambhir, S. S.; Cheng, Z.; Tian, J. First-in-human liver-tumour surgery guided by multispectral fluorescence imaging in the visible and near-infrared-I/II windows. *Nature Biomedical Engineering* **2020**, *4*, 259-271.

(34) Wang, C.; Fan, W.; Zhang, Z.; Wen, Y.; Xiong, L.; Chen, X. Advanced Nanotechnology Leading the Way to Multimodal Imaging-Guided Precision Surgical Therapy. *Adv Mater* **2019**, *31*, e1904329.

(35) Caravan, P.; Ellison, J. J.; McMurry, T. J.; Lauffer, R. B. Gadolinium(III) Chelates as MRI Contrast Agents: Structure, Dynamics, and Applications. *Chemical Reviews* **1999**, *99*, 2293-2352.

(36) Kleeff, J.; Korc, M.; Apte, M.; La Vecchia, C.; Johnson, C. D.; Biankin, A. V.; Neale, R. E.; Tempero, M.; Tuveson, D. A.; Hruban, R. H.; Neoptolemos, J. P. Pancreatic cancer. *Nature Reviews Disease Primers* **2016**, *2*, 16022.

(37) Halbrook, C. J.; Lyssiotis, C. A.; Pasca di Magliano, M.; Maitra, A. Pancreatic cancer: Advances and challenges. *Cell* **2023**, *186*, 1729-1754.

(38) Mizrahi, J. D.; Surana, R.; Valle, J. W.; Shroff, R. T. Pancreatic cancer. *Lancet* **2020**, *395*, 2008-2020.

(39) Pereira, S. P.; Oldfield, L.; Ney, A.; Hart, P. A.; Keane, M. G.; Pandol, S. J.; Li, D.; Greenhalf, W.; Jeon, C. Y.; Koay, E. J.; Almario, C. V.; Halloran, C.; Lennon, A. M.; Costello, E. Early detection of pancreatic cancer. *Lancet Gastroenterol Hepatol* **2020**, *5*, 698-710.

(40) Chauhan, V. P.; Jain, R. K. Strategies for advancing cancer nanomedicine. *Nat Mater* **2013**, *12*, 958-962.

(41) Cabral, H.; Matsumoto, Y.; Mizuno, K.; Chen, Q.; Murakami, M.; Kimura, M.; Terada, Y.; Kano, M. R.; Miyazono, K.; Uesaka, M.; Nishiyama, N.; Kataoka, K. Accumulation of sub-100 nm polymeric micelles in poorly permeable tumours depends on size. *Nature Nanotechnology* **2011**, *6*, 815-823.

(42) Chauhan, V. P.; Stylianopoulos, T.; Martin, J. D.; Popović, Z.; Chen, O.; Kamoun, W. S.; Bawendi, M. G.; Fukumura, D.; Jain, R. K. Normalization of tumour blood vessels improves the delivery of nanomedicines in a size-dependent manner. *Nat Nanotechnol* **2012**, *7*, 383-388.

(43) Shen, Y.; Goerner, F. L.; Snyder, C.; Morelli, J. N.; Hao, D.; Hu, D.; Li, X.; Runge, V. M. T1 Relaxivities of Gadolinium-Based Magnetic Resonance Contrast Agents in Human Whole Blood at 1.5, 3, and 7 T. *Investigative Radiology* **2015**, *50*.

(44) Levine, D.; McDonald, R. J.; Kressel, H. Y. Gadolinium Retention After Contrast-Enhanced MRI. *Jama* **2018**, *320*, 1853-1854.

(45) Davies, J.; Siebenhandl-Wolff, P.; Tranquart, F.; Jones, P.; Evans, P. Gadolinium: pharmacokinetics and toxicity in humans and laboratory animals following contrast agent administration. *Archives of Toxicology* **2022**, *96*, 403-429.

(46) Liu, J.; Chen, C.; Wei, T.; Gayet, O.; Loncle, C.; Borge, L.; Dusetti, N.; Ma, X.; Marson, D.; Laurini, E.; Pricl, S.; Gu, Z.; Iovanna, J.; Peng, L.; Liang, X.-J. Dendrimeric nanosystem consistently circumvents heterogeneous drug response and resistance in pancreatic cancer. *Exploration* **2021**, *1*, 21-34.

(47) Commisso, C. The pervasiveness of macropinocytosis in oncological malignancies. *Philos Trans R Soc Lond B Biol Sci* **2019**, *374*, 20180153.

(48) Yao, W.; Rose, J. L.; Wang, W.; Seth, S.; Jiang, H.; Taguchi, A.; Liu, J.; Yan, L.; Kapoor, A.; Hou, P.; Chen, Z.; Wang, Q.; Nezi, L.; Xu, Z.; Yao, J.; Hu, B.; Pettazzoni, P. F.; Ho, I. L.; Feng, N.; Ramamoorthy, V.; Jiang, S.; Deng, P.; Ma, G. J.; Den, P.; Tan, Z.; Zhang, S. X.; Wang, H.; Wang, Y. A.; Deem, A. K.; Fleming, J. B.; Carugo, A.; Heffernan, T. P.; Maitra, A.; Viale, A.; Ying, H.; Hanash, S.; DePinho, R. A.; Draetta, G. F. Syndecan 1 is a critical mediator of macropinocytosis in pancreatic cancer. *Nature* **2019**, *568*, 410-414.

(49) Wei, T.; Chen, C.; Liu, J.; Liu, C.; Posocco, P.; Liu, X.; Cheng, Q.; Huo, S.; Liang, Z.; Fermeglia, M.; Pricl, S.; Liang, X.-J.; Rocchi, P.; Peng, L. Anticancer drug nanomicelles formed by self-assembling amphiphilic dendrimer to combat cancer drug resistance. *Proceedings of the National Academy of Sciences* **2015**, *112*, 2978-2983.

(50) Allard, M.; Doucet, D.; Kien, P.; Bonnemain, B.; Caillé, J. M. Experimental study of DOTA-gadolinium. Pharmacokinetics and pharmacologic properties. *Invest Radiol* **1988**, *23 Suppl 1*, S271-274.

(51) Wiener, E. C.; Brechbiel, M. W.; Brothers, H.; Magin, R. L.; Gansow, O. A.; Tomalia, D. A.; Lauterbur, P. C. Dendrimer-based metal chelates: a new class of magnetic resonance imaging contrast agents. *Magn Reson Med* **1994**, *31*, 1-8.

(52) Luo, K.; Liu, G.; Zhang, X.; She, W.; He, B.; Nie, Y.; Li, L.; Wu, Y.; Zhang, Z.; Gong, Q.; Gao, F.; Song, B.; Ai, H.; Gu, Z. Functional L-Lysine Dendritic Macromolecules as Liver-Imaging Probes. *Macromolecular Bioscience* **2009**, *9*, 1227-1236.

(53) Li, H.; Sun, J.; Zhu, H.; Wu, H.; Zhang, H.; Gu, Z.; Luo, K. Recent advances in development of dendritic polymer-based nanomedicines for cancer diagnosis. *WIREs Nanomedicine and Nanobiotechnology* **2021**, *13*, e1670.